nanomaterials

MDPI

Article

Evaluation of Antibacterial and Plant Responses Alongside UV-Induced Dye Decolorization Using Plant Extract-Mediated Alumina Nanoparticles

Tamer Dogan [1,*] and Kagan Veryer [2]

[1] Department of Computer Technologies, Vocational School of Imamoglu, Cukurova University, 01700 Adana, Türkiye
[2] Department of Biology, Faculty of Engineering and Natural Sciences, Osmaniye Korkut Ata University, 80010 Osmaniye, Türkiye; kaganveryer@osmaniye.edu.tr
* Correspondence: tdogan@cu.edu.tr; Tel.: +90-322-338-60-84

Abstract

Urban green waste is mostly composted or used for energy, and its potential for material production remains largely untapped. Here, an aqueous extract of *Laurus nobilis* pruning waste was used to green-synthesize alumina nanoparticles (NPs), which were evaluated for dye decolorization, antibacterial activity and effects on bean seedlings. XRD indicated a cubic defect-spinel transition alumina tentatively consistent with η-Al_2O_3 (apparent Scherrer crystallite size, 7.31 nm), and SEM showed ~29 nm surface particles within micrometre-scale agglomerates. Under UV irradiation, 62.18% decolorization of Basic Fuchsin was observed after 180 min in the presence of the NPs; a catalyst-free UV control was not performed, so the contribution of direct photolysis could not be separated from nanoparticle-assisted removal, while no measurable net removal was observed in the parallel dark experiment; decolorization efficiency decreased to approximately 19% in the fifth cycle. The NPs showed no marked antibacterial activity against the tested strains at 12.5–50 mg/mL. In an exploratory assay with etiolated *Phaseolus vulgaris* seedlings, growth parameters showed no consistent dose-dependent trend, whereas pigment contents varied non-monotonically, peaking at 40 mg/L and declining at 160 mg/L. Bay laurel pruning waste can thus serve as a reaction medium for transition alumina synthesis, but the energy demand of calcination, catalyst deactivation and dose-dependent plant responses require further study.

Keywords: transition alumina; UV irradiation; dye decolorization; plant response; antibacterial

Check for updates

Academic Editor: Marco Stoller

Received: 31 October 2026
Revised: 18 November 2026
Accepted: 20 November 2026
Published: 23 November 2026

Copyright: © 2026 by the authors. Licensee MDPI, Basel, Switzerland. This article is an open access article distributed under the terms and conditions of the Creative Commons Attribution (CC BY) license.

1. Introduction

Textile dyes discharged with industrial effluents impair the aesthetic quality of water bodies, block light penetration and thereby reduce photosynthesis and dissolved oxygen levels, and can act as toxic, mutagenic and carcinogenic agents [1]. Treating such effluents is relevant to Sustainable Development Goal 6, which seeks to ensure the availability and sustainable management of water and sanitation for all, while producing materials from waste streams is relevant to Goal 12 on sustainable consumption and production patterns [2]. Green waste, which mainly arises in urban areas from the maintenance of gardens and public parks, is mostly composted or used for energy production, and its potential for material utilization remains largely untapped [3].

With the development of nanotechnology, aluminum oxide (Al_2O_3) nanoparticles (NPs) have gained significant prominence in scientific research due to their chemical stability

and broad application areas [4,5]. Plant extract-mediated synthesis provides an alternative route for preparing alumina nanoparticles [6]; however, its environmental benefit depends on the complete synthesis and thermal-treatment requirements. The environmental and biomedical performance of the synthesized nanomaterials is directly related to their size, surface properties, and crystal phase [7]. For alumina, the sequence of transition phases formed on thermal activation depends on the starting hydroxide (e.g., boehmite → γ → δ → θ → α, bayerite → η → θ → α and gibbsite → χ → κ → α-Al_2O_3) [8]. Accordingly, the final phase is determined mainly by the precursor and the thermal treatment conditions, and in green synthesis routes plant extracts have additionally been proposed to act as "capping" agents [9,10]. Green synthesis studies in the literature generally focus on the thermodynamically stable α-Al_2O_3 and cubic γ-Al_2O_3 phases, utilizing plant extracts such as clove, macroalgae, and neem in plant-mediated synthesis routes [11–17]. In contrast, the metastable η- Al_2O_3 transition phase, which can be obtained at relatively low temperatures via the green synthesis route [18,19], has been reported to a much more limited extent in the literature [6]. Alumina has been reported to possess a large specific surface area, active Lewis acid sites and a high adsorption capacity, owing to the structural disorder arising from the high tetrahedral coordination of Al^{3+} ions in its oxygen sublattice [9,19,20]. These reported features make η-Al_2O_3 a candidate not only for photocatalytic environmental remediation processes but also for pathogen-interactive biological applications addressing increasing antibiotic resistance and the pursuit of sustainable agriculture [21–23]. Although the antibacterial effects of α and γ phases with various modifications have been investigated in the literature [24,25], the antibacterial and agricultural application potential of the η-Al_2O_3 phase, characterized by its reactive surface regions, has not yet been adequately explored. A previous green route used clove extract with ultrasonic-assisted hydrothermal processing to prepare boehmite and η-alumina nanostructures [19]. The present work instead evaluates an aqueous extract of *Laurus nobilis* pruning waste as a reaction medium for cubic defect-spinel transition alumina synthesis. Its novelty concerns the pruning-waste feedstock and the integrated physicochemical and application assessment, rather than proof of a phase-selective synthesis route. The literature discusses differences in Al coordination and surface acidity among transition aluminas [9,20], but the present measurements do not establish a phase-specific density of tetrahedral Al sites or Lewis acid centres in the synthesized sample. Addressing this gap, the present work investigates the structural, optical and surface-related properties of a plant extract-mediated cubic defect-spinel transition alumina, with a tentative η-Al_2O_3 assignment (the term η-type alumina used in the biological assays denotes this same material and does not imply independent phase confirmation). Accordingly, in our study, this material was obtained using an aqueous extract of *Laurus nobilis* (bay laurel) pruning waste collected on a university campus. In the present route, the extract-derived organic matter was subjected to stepwise calcination up to 900 °C, and the weak carbon-related FT-IR bands were interpreted tentatively as trace residues or contamination; the final composition was not inferred from the properties of the source plant. In this route, the extract is regarded primarily as the reaction medium for the synthesis; whether it also acts as a capping or structure-directing agent was not established because an extract-free synthesis control was not included. The conversion of an Al(III) nitrate precursor to Al_2O_3 does not itself demonstrate a reduction of aluminium. The structural and optical properties of the synthesized nanoparticles were characterized using XRD, FTIR, SEM, and UV-Vis DRS techniques; subsequently, UV-induced dye decolorization, antibacterial activity against pathogens, and the effects of the material on plant growth and physiological responses were evaluated, and the environmental implications of the material are discussed.

2. Materials and Methods

2.1. Processing Nanoparticles with Green Synthesis Method

In this study, leaves and branches of *Laurus nobilis* L. (bay laurel) were collected from landscaping wastes resulting from pruning operations at the Osmaniye Korkut Ata University campus (Osmaniye, Türkiye). The plant material was identified by Dr. Kağan Veryer utilizing the source Flora of Turkey and the East Aegean Islands [26] as a reference, and a representative vegetative specimen was preserved for reference purposes under the code KVeryer-PL-0002. The plant material was dried in the shade at room temperature for 15 days, and then ground into powder using a plant grinder (Demsan, Istanbul, Türkiye). 10 g of the powdered plant material was weighed (Denver Instrument, Arvada, CO, USA), mixed with 500 mL of distilled water, and the extraction process was carried out at 70 °C with a constant stirring speed of 300 rpm for 2.5 h. The extract obtained at the end of the process was filtered through Whatman No. 1 filter paper (Cytiva, Little Chalfont, UK) and stored at +4 °C until use. Although limited in the extraction of lipophilic or low-polarity compounds, distilled water was preferred as the solvent in this study because it offers a low-cost and eco-friendly option for the isolation of polar compounds [27,28]. In the synthesis stage; 7.5 g of aluminum nitrate nonahydrate ($Al(NO_3)_3 \cdot 9H_2O$) (CAS: 7784-27-2) was weighed (Denver Instrument, Arvada, CO, USA) to contain 0.4 M Al^{3+} ions and added to 50 mL of the plant extract (Equation (1), schematic representation). The mixture was left to react at 70 °C with a constant stirring speed of 210 rpm for 2 h. Subsequently, the temperature was raised to 200 °C, and the stirring process was continued until the solvent completely evaporated. The solid residue formed at the end of evaporation was carefully scraped from the beaker surface and transferred to an alumina crucible. Considering that the thermal decomposition of aluminum nitrate nonahydrate proceeds through stepwise dehydration and the subsequent removal of nitrate groups [29], the precursor was calcined in a programmable muffle furnace (Protherm, Ankara, Türkiye) at a heating rate of 2 °C min^{-1}. The heat treatment was performed in three successive stages: organic burnout at 400 °C for 2 h, thermal decomposition at 700 °C for 2 h, and final calcination at 900 °C for 6 h. Assuming heating from approximately 25 °C to 900 °C at 2 °C min^{-1}, the programmed heating and dwell periods total approximately 17.3 h, excluding cooling. The 7.5 g of $Al(NO_3)_3 \cdot 9H_2O$ corresponds to approximately 0.020 mol Al and a theoretical Al_2O_3 yield of 1.02 g per batch. These values describe the programmed duration and theoretical yield, not a measured electricity consumption or isolated yield; the prolonged thermal treatment limits claims of overall sustainability.

$$Al(NO_3)_3 \cdot 9H_2O + \text{plant extract precursor} \xrightarrow{900\ ^\circ C,\ calcination} transition\ Al_2O_3\ + \text{gaseous by products} \quad (1)$$

The foamed solid obtained as a result of this process was ground into a finer powder using an agate mortar. After adding distilled water to the nanoparticle powder, the sample was centrifuged (5000 rpm, 10 min) and the resulting supernatant was removed. Distilled water was added again to the precipitate, which was then suspended using a vortex mixer (DragonLab, Beijing, China), and this centrifugation-washing process was repeated five consecutive times to reduce soluble precursor-derived residues [30–32].

The precursor was subjected to successive dwell periods at 400, 700, and 900 °C as described above. Thermal treatment can affect particle coarsening, pore volume and specific surface area [33,34], but no calcination-temperature series or BET measurements were available for the present material. Consequently, this programme cannot be regarded as an experimentally optimized route for preserving nanoscale morphology or selecting a specific transition-alumina phase.

2.2. Characterization of the Transition Alumina Nanoparticles

The characterization stage in this study was examined under three main headings: structural and chemical (XRD, FT-IR), morphological and elemental (SEM-EDX), and optical (PL, DRS) characterization. The crystal structure and lattice parameters of the samples were investigated using a PANalytical Empyrean X-ray diffractometer (PANalytical, Almelo, The Netherlands; CuKα radiation, $\lambda = 1.54060$ Å) within a 2θ scanning range of 3° to 90° with a step size of 0.01°. The chemical bonding characteristics and functional groups of the synthesized samples were analyzed using a Jasco FT/IR-6700 Fourier transform infrared (FT-IR) spectrometer (Jasco, Tokyo, Japan) in the wavenumber range of 399–4000 cm^{-1}. The surface morphology and elemental distribution of the synthesized samples were characterized using a FEI Quanta 650 Field Emission Scanning Electron Microscope (FE-SEM) equipped with an EDX detector (FEI, Hillsboro, OR, USA). PL measurements were conducted at room temperature utilizing a He-Cd laser with an excitation wavelength of 325 nm. The diffuse reflectance spectra (DRS) of the solid samples were obtained using a Shimadzu UV-3600 Plus UV-Vis spectrophotometer, whereas other UV-Vis spectroscopic measurements were acquired using a Shimadzu UV-3500 spectrometer (Shimadzu, Kyoto, Japan). UV-induced dye decolorization and its apparent kinetics were monitored using a Jasco V-730 UV-Vis spectrophotometer.

2.3. UV-Induced Dye Decolorization and Reusability Tests

Basic Fuchsin (BF) was used as the model dye in the UV-induced decolorization experiments. A 100 mL portion of BF solution with an initial concentration of 13 mg/L (initial absorbance = 1.70 ± 0.30 at λmax = 546.2 nm) and 0.1 g nanoparticle was used. No separate dark pre-equilibration step was applied before irradiation; instead, adsorption in the absence of light was assessed in a parallel experiment, in which an identical nanoparticle–dye suspension was continuously stirred in the dark for 180 min and sampled at the same 20-min intervals as the irradiated suspension. The irradiation experiments were conducted at room temperature under UV irradiation using a laboratory-scale photoreactor equipped with a 300 W OSRAM high-pressure mercury lamp (OSRAM GmbH, Munich, Germany), the configuration and emission characteristics of which were previously described by Dogan [35]. During UV irradiation, 3 mL aliquots were withdrawn from the reaction medium at 20 min intervals and centrifuged at 13,500 rpm (approximately 13,450× *g*) for 10 min using a centrifuge (Hettich, Tuttlingen, Germany) to separate suspended photocatalyst particles from the liquid phase. Following centrifugation, the UV–Vis spectra of the supernatants were recorded over the 350–800 nm wavelength range using a UV–Vis spectrophotometer (Jasco V-730, Hachioji, Tokyo, Japan). The decrease in absorbance at the characteristic maximum of BF (λmax = 546.2 nm) was used to quantify decolorization. A catalyst-free BF solution irradiated under otherwise identical conditions (UV-only control) was not tested; therefore, direct photolysis and nanoparticle-assisted removal could not be resolved. No mineralization or degradation-product analysis was performed. Five consecutive irradiation cycles (the initial use followed by four reuse cycles) were performed under the reported reaction conditions to assess the change in apparent decolorization performance on reuse. Recovery yield and recovered catalyst mass were not determined, so equal catalyst loading across reuse cycles could not be verified. Between consecutive irradiation cycles, the remaining reaction mixture was placed in an oven at 70 °C overnight until the solvent had completely evaporated. A fresh 100 mL portion of BF solution was then added to the retained solid residue for the next cycle. No separate particle-isolation or washing step was performed between cycles.

2.4. Plant Material and Sterilization

The seed surface sterilization and imbibition procedure was performed with modifications to previously described seed sterilization protocols [36]. Seeds of *Phaseolus vulgaris* L., a commercially important crop species, were obtained from a local market in Osmaniye Province, Türkiye. The seeds were initially washed with tap water and subsequently handled under sterile conditions. They were briefly rinsed with 70% ethanol, which was immediately decanted without any incubation period. The seeds were then surface-sterilized by agitation in approximately 0.5% sodium hypochlorite solution for 5 min, followed by three rinses with sterile distilled water. After surface sterilization, the seeds were immersed in sterile distilled water and maintained in a sealed sterile container for 5 h to allow imbibition.

2.5. Antibacterial Assay

The antibacterial activity of η-type alumina NPs against three bacterial strains, *Bacillus cereus BC6830* (K9), *Escherichia coli* NCTC 9001 (K51) and *Staphylococcus aureus* BC7231 (K57), was evaluated using the Kirby–Bauer disc diffusion method. The bacterial strains were grown in Nutrient broth (Sigma-Aldrich, St. Louis, MO, USA), and the turbidity of each bacterial inoculum was adjusted to 0.50 ± 0.05 McFarland using a densitometer (DEN-1B, Biosan, Riga, Latvia). The standardized inocula were transferred to sterile Petri dishes and subsequently distributed uniformly over the entire surface of Mueller–Hinton agar (MHA; Sigma-Aldrich, St. Louis, MO, USA) using sterile cotton swabs. Sterile 6-mm blank discs (Bioanalyse, Ankara, Türkiye) were impregnated with 30 µL of η-type alumina NP suspensions (sonicated (Ram Scientific, Mumbai, India) in distilled and sterile water) at concentrations of 50, 25, and 12.5 mg/mL. Sterile distilled water was used as the negative control, while gentamicin was used as the positive control. The discs were placed on the inoculated MHA plates, which were then incubated at 36.5 °C for 24 h. Following incubation, the inhibition-zone diameters were measured in millimetres using a ruler.

2.6. Plant Growth and Physiological Response Assay

The assay was performed with modifications based on the method described by Sedefoglu et al. [37]. Six surface-sterilized seeds were placed in sterile 9-cm glass Petri dishes containing two layers of autoclaved Whatman No. 1 filter paper. Each Petri dish was considered an individual replicate, and each treatment was conducted in triplicate, with six seeds per replicate. η-type alumina NP suspensions were freshly prepared in distilled water and sonicated before application. Subsequently, 10 mL of the nanoparticle suspensions at concentrations of 0, 10, 20, 40, 80, and 160 mg/L was added to each Petri dish. The Petri dishes were sealed with parafilm and incubated at 25 °C under dark conditions for 7 days. At the end of the incubation period, root and shoot lengths were measured in millimetres, and fresh weights were determined; harvesting, measurements and leaf sampling were carried out under standard laboratory lighting for approximately 8 min per treatment, in the same way for all treatments.

For pigment analysis, the leaves of all seedlings from the three Petri dishes of each treatment were pooled, and 100 mg of this pooled fresh leaf tissue was extracted with 10 mL of cold 80% acetone in the dark. Following extraction, the samples were centrifuged (3000 rpm for 5 min), and the absorbance of the supernatants was measured at 450, 537, 645, and 663 nm using a UV–Vis spectrophotometer (Jasco V-730, Hachioji, Tokyo, Japan). Chlorophyll a, chlorophyll b, total chlorophyll, total carotenoid, and anthocyanin contents were calculated from the corresponding absorbance values using the equations given below. Chlorophyll a (Equation (2)), chlorophyll b (Equation (3)), total chlorophyll (Equation (4)), and total carotenoid (Equation (5)) contents were expressed as mg g^{-1} fresh weight (FW), whereas anthocyanin (Equation (6)) content was expressed as µmol g^{-1} FW. In the equations, A

represents the absorbance at the indicated wavelength, V represents the extract volume (mL), and W represents the fresh tissue weight (g).

$$Chl\ a = (12.7A\ 663 - 2.69A\ 645) \times V/(1000W) \quad (2)$$

$$Chl\ b = (22.9A\ 645 - 4.86A\ 663) \times V/(1000W) \quad (3)$$

$$Total\ Chl = (20.2A\ 645 + 8.02A\ 663) \times V/(1000W) \quad (4)$$

$$Total\ carotenoid = 4.07A\ 450 - (0.0435\ Chl\ a + 0.367\ Chl\ b) \quad (5)$$

$$Anthocyanin = (0.08173A\ 537 - 0.00697A\ 645 - 0.002228A\ 663) \times V/W \quad (6)$$

For dry-weight determination, the seedlings were dried in a drying oven (Memmert, Schwabach, Germany) at 70 °C until a constant weight was reached and subsequently weighed.

2.7. Statistical Analysis

Antibacterial assay data were expressed as mean ± standard deviation (SD). Differences among η-type alumina NP treatments for plant growth and biomass parameters were evaluated using one-way analysis of variance (ANOVA), followed by Duncan's multiple range test. Pigment contents were determined from a single pooled extract per treatment and evaluated descriptively. Antibacterial assays were performed in triplicate. Differences were considered statistically significant at $p < 0.05$. The distribution of SEM-derived size measurements was additionally assessed using the Shapiro–Wilk normality test. Both raw and logarithmically transformed size data were tested to evaluate their compatibility with normal and lognormal distributions, respectively. Statistical analyses were performed using SPSS Statistics version 18.0 (SPSS Inc., Chicago, IL, USA), while graphical analyses were carried out using Origin 8.1 (OriginLab Corporation, Northampton, MA, USA).

3. Results and Discussion

3.1. XRD Analysis

The X-ray diffraction pattern exhibits broad reflections indexed to the (111), (220), (311), (222), (400), (511), and (440) planes of a cubic defect-spinel transition alumina framework (Fd3m space group) (Figure 1). Distinguishing among structurally related transition aluminas (η- and γ-phases) requires careful evaluation of peak profiles. While γ-Al_2O_3 commonly undergoes slight tetragonal distortion (c/a < 1) resulting in doublet splitting or notable asymmetry at the (400) reflection (~45.8° 2θ), the observed pattern displays a singular, symmetric (400) profile centered at 2θ = 45.8351° (d = 1.98 Å), which is consistent with the cubic oxygen framework of η-Al_2O_3 [38,39]. Furthermore, no diagnostic reflections for δ-, θ-, or rhombohedral α-Al_2O_3 were detected. Nevertheless, since XRD alone cannot unambiguously distinguish η- from γ-like defect-spinel alumina at such small crystallite sizes, the material is described as a cubic defect-spinel transition alumina tentatively consistent with η-Al_2O_3 and is referred to as cubic defect-spinel transition alumina in the physicochemical discussion; an independent phase-sensitive technique (e.g., ^{27}Al MAS NMR or SAED) would be required to confirm this assignment. These phase-sensitive measurements were not performed in the present study. Moreover, η-Al_2O_3 is usually formed from crystalline bayerite at considerably lower temperatures, whereas the present material was obtained from a nitrate-derived precursor after calcination at 900 °C. The presence of a cubic spinel-type pattern at this temperature is therefore not in itself evidence for η-Al_2O_3, and thermal analysis of the precursor together with XRD of samples calcined at different temperatures would be required to clarify the phase evolution.

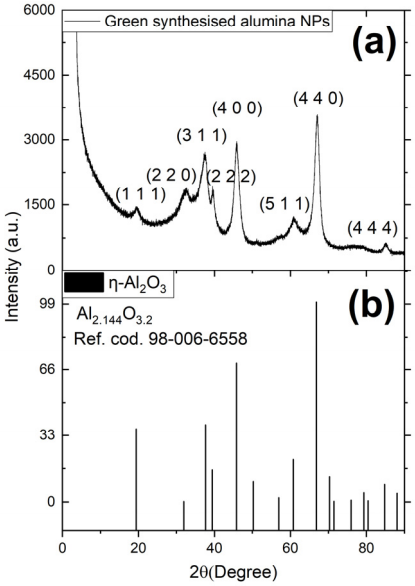

Figure 1. (**a**) XRD pattern of the synthesized cubic defect-spinel transition alumina and (**b**) the η-Al_2O_3 reference pattern (reference code 98-006-6558) used for comparison. Similarity to this reference does not independently distinguish η- from γ-like transition alumina.

Primarily, each 2θ (Bragg angle) peak position obtained from the XRD instrument was applied to the Bragg's Law equation ($d = \lambda/2\sin\theta$), which provides the distance between crystal planes (d-spacing). In this equation, the wavelength was taken as $\lambda = 1.54056$ Å (Cu-Kα). The indexed reflections were evaluated using a cubic defect-spinel framework; this indexing is not an independent confirmation of η-Al_2O_3. In a cubic crystal system, the mathematical relationship among the interplanar spacing (d), lattice parameter (a), and Miller indices (hkl) is defined by the following formula (Equation (7)):

$$d = \frac{a}{\sqrt{h^2 + k^2 + l^2}} \quad (7)$$

The *a* values were calculated for the individual reflections using the above equation. In the study by Tilley and Eggleton [39], the differential XRD and selected area electron diffraction (SAED) data of the η-alumina phase obtained from Andoom bauxite were compared. In that study, the characteristic peaks of η-alumina were calculated as 4.6 Å for the (111) plane, 2.8 Å for (220), 2.40 Å for (311), 2.27 Å for (222), 1.97 Å for (400), and 1.40 Å for (440). The d-spacing values calculated from the XRD data obtained in the present study are in good agreement with the theoretical [40] and experimental [39] reference values. The average lattice parameter (*a*avg) of the transition alumina synthesized in this study is 7.8908 Å. For cubic transition alumina phases (η and γ), the cell parameter *a* ranges between 7.90 and 7.95 Å in the literature Zhou and Snyder [41]. The calculated value of 7.8908 Å is slightly below this range and therefore does not by itself discriminate between the η and γ phases. The origin of this small deviation was not determined; the lattice parameter alone does not identify strain, residual surface species or a specific alumina polymorph.

The crystallite size (coherent diffraction domain size) of the synthesized sample was initially evaluated using the Debye–Scherrer equation ($D = k\lambda/\beta\cos\theta$), where the shape factor (k) was taken as 0.9. The FWHM values were not corrected for instrumental broadening and may include strain and overlap contributions; therefore, the Scherrer sizes are apparent estimates rather than separately resolved physical domain sizes. For the seven principal indexed reflections, the reported arithmetic mean is 7.31 nm and the median is 4.93 nm. Including the tentative high-angle (444) feature gives an arithmetic mean of 6.45 nm; this feature is excluded from the principal summary because of its very large width. The seven-

reflection mean is 7.31 ± 3.22 nm (standard error of the mean). Weighting these seven estimates by the peak heights listed in Table 1 gives 6.19 nm; this is a peak-height-weighted summary, not a measured particle-population mean. The substantial reflection-to-reflection dispersion in the Scherrer crystallite sizes (ranging from 1.60 nm to 25.97 nm) may reflect crystallographic strain anisotropy, together with peak overlap and uncertainties in profile fitting of the broad reflections. Because the unweighted mean is strongly influenced by the comparatively narrow (222) reflection, the median value (4.93 nm) is considered more representative of the typical coherent domain size.

Table 1. XRD Peak Analysis and Crystallite Size Calculation.

2θ (°)	**Peak Height (cts)**	**FWHM Left (°2θ)**	**d (Å)**	**hkl**	**Apparent D (nm)**	**$1/D^2$ (10^{16} m^{-2})**
3.01	2632.69	1.124	29.31	Unassigned	-	-
19.59	166.06	1.069	4.53	(111)	7.54	1.76
32.29	517.27	5.18	2.77	(220)	1.60	39.06
37.33	1176.68	2.70	2.41	(311)	3.10	10.41
39.61	459.74	0.33	2.27	(222)	25.97	0.15
45.84	1320.27	1.75	1.98	(400)	4.93	4.11
61.02	432.17	5.41	1.52	(511)	1.70	34.60
66.93	1959.04	1.50	1.40	(440)	6.34	2.49
83.01	160.01	24.46	1.16	(444)	0.43	-

Note: The parameter δ is calculated via the empirical relation $\delta = 1/D^2$ to provide a qualitative inverse-square scaling of domain sizes; it does not represent a direct physical measurement of dislocation lines or specific defect concentrations.

In this method, the entire XRD peak broadening is attributed solely to the crystallite size; that is, the microstrain (ε) is assumed to be 0, lattice defects are ignored, and it is assumed that dislocations and internal stresses do not contribute to the peak broadening.

The apparent Scherrer sizes from the (111), (400), and (440) reflections range from approximately 4.9 to 7.5 nm, consistent with nanoscale coherent diffraction domains. Gholizadeh et al. [19] reported 3.6–4.2 nm crystallite sizes for their clove-extract route, although differences in phase, thermal treatment and peak analysis preclude a direct ranking of synthesis routes. Peak broadening in the present material may include finite-size, strain and disorder contributions and does not quantify specific defect populations.

An inverse-square domain-size metric was calculated using:

$$\delta = 1/D^2 \quad (8)$$

Here, D is the Scherrer crystallite size in metres, and δ is expressed in m^{-2} (Equation (8)). This empirical metric increases as the estimated domain size decreases; it is not a direct measurement of dislocation density, domain-boundary density, or point-defect concentration. Accordingly, the values reported in Table 1 should be interpreted only as an inverse-square scaling of the Scherrer domain sizes.

Oxygen and cation vacancies are point defects, whereas dislocations and planar stacking faults are extended defects. The present XRD line-broadening analysis does not separately quantify these defect populations or establish their preferential concentration along a particular crystallographic direction. The high-angle diffraction feature at $2\theta = 83.0149°$ was tentatively indexed to the (444) reflection of the cubic defect-spinel framework; owing to its very large width, it was not used for further analysis. Apart from the unassigned low-angle feature discussed below, no reflections attributable to θ- or α-Al_2O_3 or to other crystalline secondary phases were detected.

Because instrumental broadening was not corrected and a Williamson–Hall plot constructed from the same peak widths showed no meaningful linear relationship ($R^2 \approx 0.015$),

the crystallite size and lattice strain contributions to peak broadening were not separated quantitatively in the present study, and the marked broadening together with the large reflection-to-reflection variation in peak width is therefore discussed only qualitatively, as it may arise from small coherent diffraction domains, inhomogeneous lattice strain and the structural disorder characteristic of transition aluminas.

In addition, it is known that η-alumina is inherently a semi-crystalline transition phase possessing cation vacancies and a defective spinel structure. Dislocations and planar stacking faults in the lattice of η-alumina can create local irregularities in the atomic arrangement, contributing to peak broadening [20]. The low-angle feature observed at $2\theta = 3.0125°$ ($d \approx 29.3$ Å) lies at the lower limit of the scanned range and could not be assigned. Its position at the scan boundary permits an instrumental contribution, but neither this possibility nor layered or organic residues were tested independently. This unassigned feature was excluded from phase indexing and Scherrer analysis, and the data do not establish high phase purity.

3.2. FT-IR Analysis

When the FT-IR spectrum is examined (Figure 2), a broad band is observed on the left side of the spectrum in the region of 3000 cm^{-1} and above. This broad band around 3350 cm^{-1} is attributed to physically adsorbed water molecules and hydrogen-bonded O–H groups within the structure [39], a characteristic observed in green synthesis studies [19]. The peak observed around 1630 cm^{-1} in the reference study [39], which is generally monitored in the 1600–1700 cm^{-1} range in the literature, indicates H–O–H bending vibrations; this is consistent with adsorbed moisture but does not quantify surface-active sites or wettability [19,39]. In particular, the deep drop around 600–800 cm^{-1} confirms that the fundamental aluminum oxide structure is dominant. Additionally, the weak peaks observed around 1000 cm^{-1} and 1250 cm^{-1} are consistent with Al–O–H bending and Al–O bond vibrations, respectively [42]. Furthermore, the weak peaks observed around 2923 cm^{-1} and 2852 cm^{-1} (C–H stretching vibrations) suggest the presence of trace carbonaceous residues, possibly originating from the plant extract or from adventitious contamination. Given the high calcination temperature (900 °C), these features are not attributed to intact phytochemical capping layers, and the FT-IR data do not provide evidence for a capping role of the extract. Meanwhile, the weak band at 2322 cm^{-1} falls within the spectral range where residual atmospheric CO_2 typically creates background subtraction artifacts; therefore, it is tentatively assigned to physisorbed ambient CO_2 or uncompensated atmospheric background subtraction rather than confirmed chemisorption on Lewis acid sites. In addition, the band at 1571 cm^{-1} falls within the 1500–1630 cm^{-1} region in which aromatic ring skeletal and C=C stretching vibrations of plant-derived compounds have been reported for plant extract-mediated Al_2O_3 NPs [43], and within the region attributed by Saleh et al. [15] to the characteristic stretching vibrations of carbonyl/carboxyl groups (C=O); it is therefore tentatively attributed to trace carbonaceous residues, although a contribution from surface carbonate species cannot be excluded.

3.3. SEM-EDX Analysis

Transition aluminas are reported to possess irregular surface structures arising from the arrangement of Al–O coordination polyhedra [8]; however, atomic-scale surface roughness, surface-defect density and specific surface area were not measured in the present study. In the study by Farajimotlagh [44], it was observed that the sizes of the NPs synthesized in an ethanol medium were larger than those obtained in water and methanol media ($51 > 37$ nm) due to limited oxidation. The SEM-derived surface-particle sizes were measured from the

SEM micrographs using the Fiji (ImageJ distribution, 1.54r, NIH, Bethesda, MD, USA) software (Figure 3a,c).

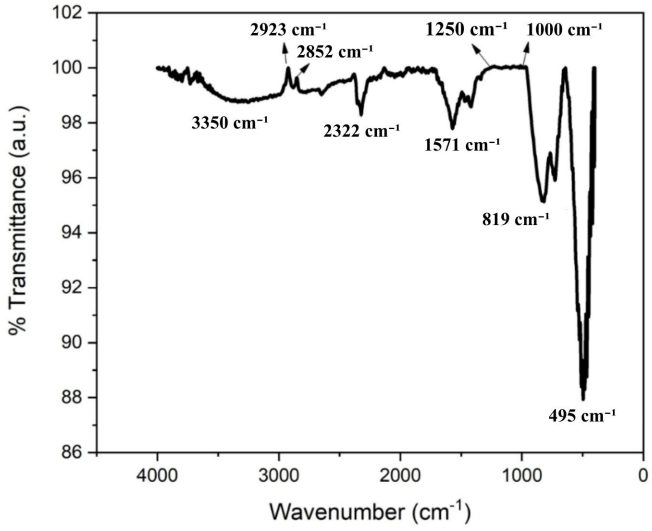

Figure 2. FT-IR analysis of NPs.

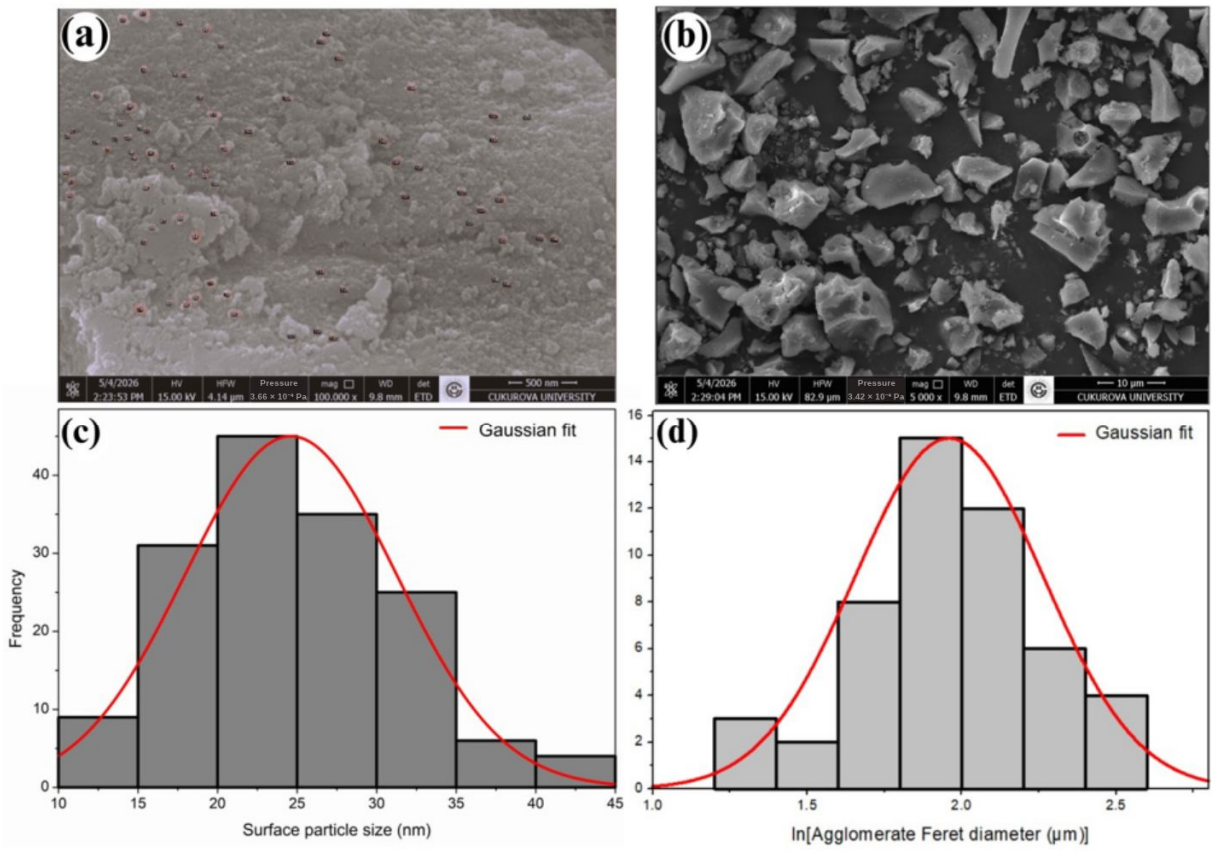

Figure 3. Multiscale SEM-based morphological analysis of cubic defect-spinel transition alumina nanoparticles: (**a**) high-magnification SEM micrograph showing nanoscale surface particles used for size measurements, (**b**) low-magnification SEM micrograph showing micrometre-scale agglomerated structures, (**c**) SEM-derived surface particle-size distribution with Gaussian fit, and (**d**) distribution of ln-transformed agglomerate Feret diameters with Gaussian fit.

The SEM-derived surface particle-size distribution obtained from 155 measurements had a mean size of 29.02 ± 7.83 nm and a median (D50) of 28.73 nm. The coefficient of

variation (CV) was 27.0% (Equation (9)). The D10, D50, and D90 values were 18.98, 28.73, and 39.27 nm, respectively, and the distribution span was 0.71 (Equation (10)).

$$CV(\%) = \frac{SD}{Mean} \times 100 \quad (9)$$

$$Span = \frac{D_{90} - D_{10}}{D_{50}} \quad (10)$$

CV: coefficient of variation; SD: standard deviation; Mean: arithmetic mean of the corresponding size measurements. D10, D50, and D90 represent the 10th, 50th, and 90th percentiles of the corresponding SEM-derived size distribution, respectively.

The SEM-derived surface particle-size measurements did not significantly deviate from normality according to the Shapiro–Wilk test ($W = 0.9857$, $p = 0.1099$). Accordingly, a Gaussian distribution curve was superimposed on the surface particle-size frequency histogram for graphical representation.

At lower magnification, the cubic defect-spinel transition alumina sample exhibited heterogeneous and irregular micrometre-scale agglomerated structures. Quantitative analysis of 50 individually delineated agglomerates yielded a mean maximum Feret diameter of 7.43 ± 2.29 µm and a median (D50) of 7.00 µm. The D10, D50, and D90 values were 4.96, 7.00, and 10.55 µm, respectively. The corresponding CV and distribution span were 30.9% and 0.80.

In contrast to the nanoscale surface particle measurements, the raw agglomerate Feret diameters significantly deviated from normality according to the Shapiro–Wilk test ($W = 0.9451$, $p = 0.0215$). Following natural logarithmic transformation, the distribution no longer showed a significant deviation from normality ($W = 0.9857$, $p = 0.8029$). Therefore, a Gaussian curve was superimposed on the frequency distribution of the ln-transformed agglomerate Feret diameters shown in Figure 3b,d.

Together, the SEM observations demonstrate a hierarchical morphology in which nanoscale surface particles are associated with larger, irregular micrometre-scale agglomerated structures.

The elemental composition of the cubic defect-spinel transition alumina was examined by EDX using the Quanta 650 FE-SEM (Figure 4), at 20 kV, a live time of 30 s and a take-off angle of 34.8°, with the eZAF Smart Quant correction procedure. The nanopowder was mounted on carbon adhesive tape and sputter-coated with Au. To match the displayed instrument table, the Au-inclusive values are reported: Al, 51.23 wt% (37.99 at%); O, 35.30 wt% (44.15 at%); C, 10.54 wt% (17.55 at%); and Au, 2.93 wt% (0.30 at%). No Au-excluded renormalization is applied to these reported values. The Al/O atomic ratio is approximately 0.860 (37.99/44.15), compared with 0.667 for ideal Al_2O_3. Because the carbon tape, coating, mounting geometry and EDX quantification affect the measured composition, these data are treated as the reported elemental analysis and do not establish intrinsic carbon content, surface stoichiometry or an oxygen-vacancy concentration.

3.4. Photoluminescence (PL) Spectroscopy

The PL spectrum was acquired at room temperature using 325 nm excitation. The exported dataset contains 667 wavelength–intensity pairs spanning 325–1000 nm. Figure 5 displays all recorded pairs as discrete symbols, without point deletion, replacement, interpolation or smoothing. The spectrum is evaluated descriptively without Gaussian deconvolution or assignment of individual fitted components.

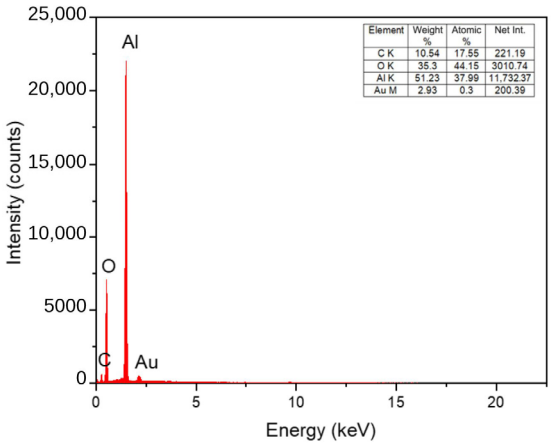

Figure 4. EDX spectrum and Au-inclusive elemental quantification of the cubic defect-spinel transition alumina, acquired at 20 kV, 30 s live time and a 34.8° take-off angle using the eZAF Smart Quant procedure. The sample was mounted on carbon tape and coated with Au; the displayed C and Au signals therefore include preparation-related contributions. The weight and atomic percentages are reported on the same basis as the table shown in the figure.

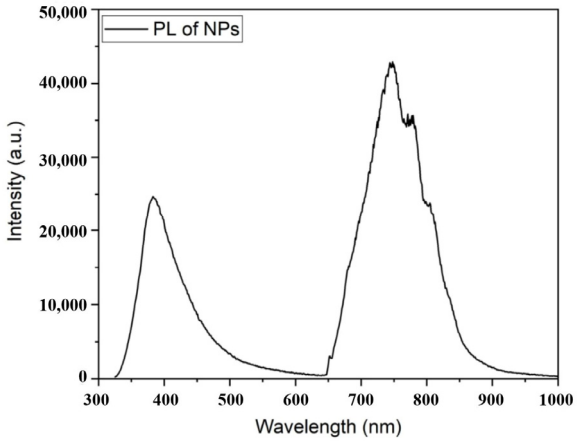

Figure 5. PL spectrum of the cubic defect-spinel transition alumina recorded at room temperature under 325 nm excitation. Discrete symbols represent all 667 recorded data pairs; no connecting lines or fitted curves are shown. The local irregularity near 453 nm and the long-wavelength band near 748 nm are retained.

The UV–visible emission band has its maximum sampled intensity at 382.798 nm (approximately 383 nm). Defect-related luminescence is a possible interpretation, but the present spectrum does not uniquely identify the emitting centres or determine their concentrations. A local intensity irregularity occurs near 453 nm, including the lower recorded values at 452.764 and 453.778 nm. These points are retained as measured. Their origin cannot be determined from the available data, and the irregularity is not assigned to a separate emission component or treated as a confirmed instrumental error.

The strongest long-wavelength signal occurs at 747.838 nm (approximately 748 nm). Its origin cannot be established from the present dataset, and an instrumental contribution, including second-order diffraction, cannot be ruled out. This band is retained in Figure 5, but no specific defect-centre assignment or mechanistic conclusion is based on it. The original sample is no longer available; therefore, repeat measurements and validation using order-sorting optics could not be performed. The unresolved origin of this feature remains a limitation of the PL analysis.

3.5. UV-VIS Spectroscopy

As the first step of the experimental optical characterization, the Diffuse Reflectance Spectroscopy (DRS) graph of the synthesized sample was examined (Figure 6a). Since no $BaSO_4$ reference baseline was recorded, absolute reflectance values could not be determined; the diffuse reflectance spectrum was therefore normalized to its maximum value (Figure 6a), and the subsequent analysis was performed on this relative reflectance. The reflectance reaches its maximum at around 370 nm (~3.35 eV), corresponding to the spectral region of lowest optical absorption of the sample. The sample underwent successive dwell periods at 400, 700, and 900 °C. The observed spectral variation may be consistent with sub-bandgap absorption. However, DRS alone does not establish whether this heat-treatment program produced or preserved specific point defects, such as oxygen vacancies, or quantify their concentrations. Beyond this limit, the decrease in reflectance toward the visible region (400–550 nm range) may be associated with sub-bandgap absorption involving localized states; its origin was not identified in the present study. Furthermore, the sharp vertical step-discontinuity observed at ~860–870 nm (centered near 863 nm) is treated as a possible instrumental changeover discontinuity rather than assigned to an intrinsic optical transition. The precise changeover setting was not documented and should not be inferred from this spectrum alone.

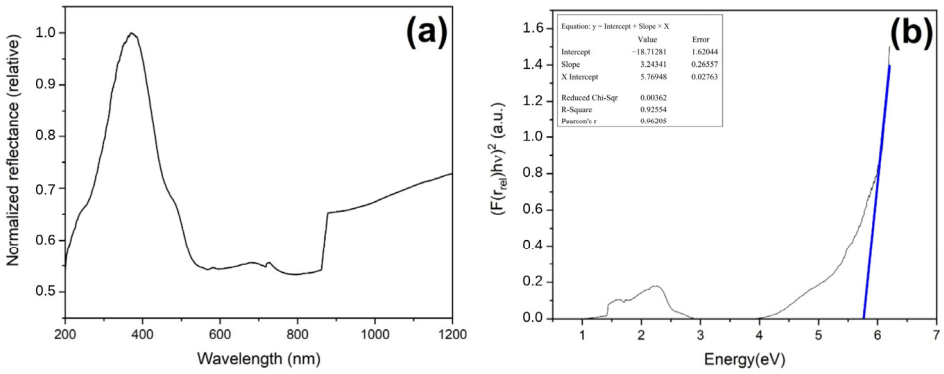

Figure 6. (**a**) Diffuse reflectance normalized to the spectrum maximum (dimensionless ratio Rrel = R/Rmax) and (**b**) the exploratory direct-Tauc representation calculated from this relative spectrum. The extrapolated intercept is 5.77 eV and is not a validated fundamental band gap; the fit is restricted to approximately 6.0–6.2 eV.

The Kubelka–Munk expression [45] was used as an exploratory transform of the relative diffuse reflectance to construct a Tauc-type representation [46]. For an optically thick scattering sample, the conventional relation is:

$$F(R_\infty) = \frac{K}{S} = \frac{(1 - R_\infty)^2}{2R_\infty} \quad (11)$$

In the conventional expression, R_∞ denotes absolute diffuse reflectance from an optically thick sample, and K and S are the absorption and scattering coefficients. Here, only Rrel = R/Rmax was available, and substituting Rrel into Equation (11) gives a relative proxy rather than a calibrated K/S value. Because the transformation is nonlinear, normalization does not merely apply a constant vertical scaling; it also sets the transformed value to zero at the reflectance maximum near 370 nm. The exploratory plot uses $[F(\mathrm{Rrel})h\nu]^2$ versus photon energy. Extrapolation of the displayed interval at approximately 6.0–6.2 eV (200–207 nm) gives an intercept of 5.77 eV. This direct-transition representation was selected for comparison with previous plant-mediated alumina reports [13,43], not because the transition type was independently established. The fit lies near the short-wavelength edge of the displayed data, and the validated operating range of the actual DRS accessory was

not documented. Combined with the assumptions of optical thickness and approximately wavelength-independent scattering, these limitations prevent treating 5.77 eV as a confirmed intrinsic band gap. The indirect representation was sensitive to the selected interval and did not yield a reliable estimate.

3.6. UV-Induced Dye Decolorization and Reuse Performance

Surface hydroxyl groups and Lewis acid sites discussed for transition aluminas [9,19,20] may affect dye–surface interactions. However, these properties were not quantified in the present sample, and neither its tentative phase assignment nor its PL/DRS response establishes the mechanism of UV-induced BF decolorization.

Absorbance was monitored at 20 min intervals over 180 min (Figure 7a). In the parallel dark experiment, the endpoint absorbance at approximately 546 nm was 0.07 above its initial value. This small increase does not demonstrate net dye uptake; residual scattering, measurement variability or suspension inhomogeneity are possible contributions, but their relative effects were not determined. No measurable net decolorization was observed in this dark test. Because a separate dark pre-equilibration step was not applied, the test does not establish that adsorption equilibrium had been reached before UV irradiation. A catalyst-free UV-only experiment was not performed; consequently, the observed UV-induced decolorization cannot be apportioned between direct photolysis and nanoparticle-assisted removal. The reported 62.18% therefore describes total decolorization in the nanoparticle-containing irradiated suspension, not the independently quantified catalytic contribution.

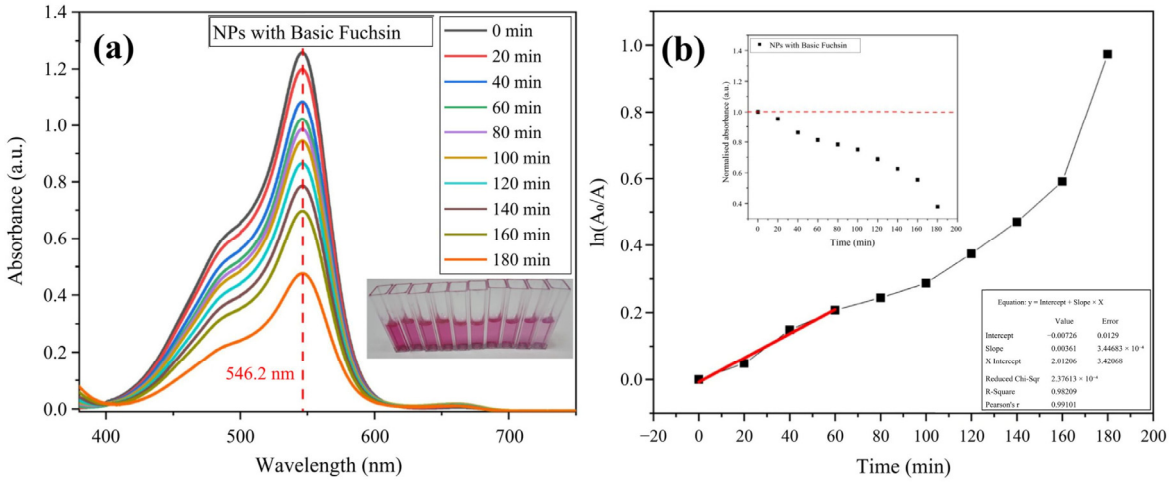

Figure 7. (**a**) UV–visible absorption spectra of BF during irradiation in the presence of the nanoparticles (inset: photographed dye solutions) and (**b**) $\ln(A_0/A_t)$ versus time, with the apparent pseudo-first-order fit restricted to 0–60 min (red line). The inset in (**b**) shows normalized absorbance A_t/A_0, not percentage removal.

The apparent pseudo-first-order relation was fitted only to the 0–60 min interval, where $\ln(A_0/A_t)$ was approximately linear ($R^2 = 0.982$), yielding k_app = 3.61×10^{-3} min^{-1} (Figure 7b). This interval contains the initial four sampling times (0, 20, 40 and 60 min) and provides a local description rather than a validated model for the full reaction. The complete 180 min profile is nonlinear: the increase is relatively slower during 60–100 min and becomes more pronounced at later times. The origin of this behaviour was not investigated. Adsorbed intermediates [47] or transport within the micrometre-scale agglomerates (Section 3.3) are possible contributors, but no mechanistic assignment is established. Because photolysis was not independently measured, k_app describes the overall observed decolorization under the stated conditions and is not an isolated catalytic rate constant.

After 180 min of UV irradiation in the presence of the cubic defect-spinel transition alumina, BF decolorization reached 62.18%, as evaluated from the absorbance decrease at 546.2 nm. This measurement does not establish complete dye mineralization or identify the degradation products. For comparison, Tebbi et al. [48] investigated TiO_2–SiO_2–Fe_2O_3 heterojunctions for Rhodamine B removal under visible light and sunlight, including catalyst-free photolysis and dark-equilibration experiments. That study provides useful methodological context, but its removal percentages cannot be used to rank the present alumina because the dye, catalyst composition and illumination conditions differ.

The reuse performance of the cubic defect-spinel transition alumina was assessed over five irradiation cycles, with the first cycle representing initial use. The decolorization efficiency decreased from approximately 62% in the first cycle to 38%, 26%, 24%, and 19% in the second, third, fourth, and fifth cycles, respectively (Figure 8a). When the decolorization performance of the first cycle was normalized to 100%, approximately 61%, 41%, 38%, and 31% of the initial activity was retained during the subsequent cycles (Figure 8b), corresponding to activity losses of approximately 39%, 59%, 62%, and 69%, respectively. Retention is calculated as DE_n/DE_1, whereas Equation (12) defines the decolorization efficiency for an individual cycle (DE_n: decolorization efficiency at 180 min in the DE-th cycle; DE_1: decolorization efficiency at 180 min in the first cycle). Although measurable decolorization performance was retained throughout all five cycles, the progressive decrease from approximately 62% to 19% indicates a substantial loss of observed performance during repeated use, without separating intrinsic deactivation from catalyst loss.

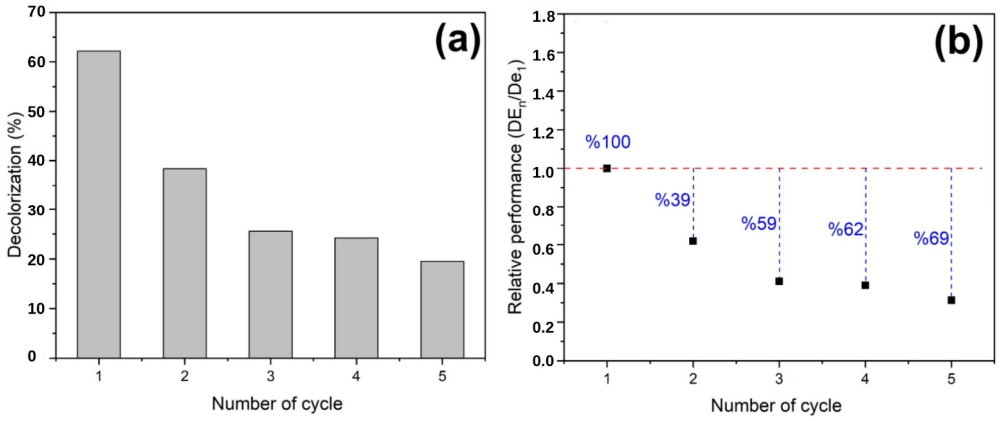

Figure 8. (**a**) BF decolorization after 180 min in each irradiation cycle and (**b**) retained relative decolorization performance DE_n/DE_1, where DE_n is the endpoint decolorization in cycle n. Dashed annotations indicate percentage loss relative to the first cycle; the ordinate in (**b**) is a dimensionless ratio, with 1.0 corresponding to 100% retention.

The absorbance-based decolorization efficiency for each cycle was calculated using Equation (12):

$$Efficiency\% = \frac{A_0 - A_t}{A_0} \times 100 \quad (12)$$

Here, A_0 and A_t are the initial and time-t absorbance values at 546.2 nm for the same cycle, and $DE = (A_0 - A_t)/A_0 \times 100$ (DE is the decolorization efficiency (%)). This absorbance-based quantity is used as a decolorization measure; a concentration-based interpretation would additionally require an applicable absorbance–concentration calibration.

The endpoint decolorization decreased from approximately 62% to 19% over the five cycles, leaving roughly 31% of the first-cycle performance. Adsorbed reaction products and physical material loss during recovery are possible explanations, but catalyst recovery yield, recovered mass and post-cycle structural or surface characterization were not

determined. These data therefore demonstrate limited retention of observed decolorization performance, while the separate contributions of intrinsic deactivation and handling losses remain unresolved.

3.7. Antibacterial Assays

The antibacterial activity of η-type alumina NPs was evaluated at concentrations of 50, 25, and 12.5 mg/mL. The results indicated that η-type alumina NPs did not exhibit a marked antibacterial effect against the tested bacterial strains. Moreover, no dose-dependent response was observed, and the differences among the tested concentrations were statistically non-significant ($p > 0.05$). Gentamicin, used as the positive control, produced clear inhibition zones ranging from 18 to 25 mm. The corresponding data are provided in Supplementary Table S1.

The limited antibacterial activity observed in the present study is consistent with previous reports of weak [49] or strain-dependent [50] antibacterial activity of Al_2O_3 NPs, although a substantial effect of α-Al_2O_3 NPs on four bacterial strains has also been reported [24]. These findings are therefore limited to the tested disc-diffusion conditions and do not exclude antibacterial activity under different dispersion or exposure conditions. Complementary MIC/MBC or direct-contact assays may provide further insight into the antibacterial potential of the nanoparticles.

Agglomeration may also have contributed to the limited inhibition: the surface particles (29.02 ± 7.83 nm) were associated with irregular micrometre-scale agglomerates (mean maximum Feret diameter, 7.43 ± 2.29 μm; Section 3.3), and agglomeration has been reported to reduce antibacterial activity by decreasing the accessible particle surface and limiting interactions between nanoparticles and bacterial cells [51,52]. In disc-diffusion assays, such agglomerates may also migrate poorly through the agar. As the aggregation state and surface charge of the nanoparticles in the test suspensions were not measured, this remains a possible contributing factor rather than a demonstrated mechanism.

From a sustainability perspective, the absence of marked inhibition in this assay is not necessarily a disadvantage. Metal and metal oxide nanoparticles released into soil have been reported to adversely affect the activity, abundance and diversity of soil microbial communities [53], so a material that does not markedly inhibit the tested strains may be preferable in applications involving possible release to soil, such as agriculture. However, only three bacterial strains were tested by disc diffusion, and effects on environmental microbial communities were not assessed and require direct testing.

3.8. Plant Growth and Physiological Responses

3.8.1. Growth and Biomass Parameters

Growth and biomass parameters exhibited heterogeneous responses to η-type alumina NP exposure. Root and shoot length, fresh weight, and dry weight did not show a consistent concentration-dependent pattern across the tested treatments. Although the 160 mg/L treatment generally resulted in lower growth and biomass values, suggesting a possible phytotoxic tendency at the highest concentration, statistical analysis did not reveal a consistent significant dose-dependent trend. Comparable variable growth responses to Al_2O_3 NP exposure have also been reported in previous studies, in which different morphological parameters responded differently across concentration ranges [54,55]. These findings indicate that plant growth responses to Al_2O_3 NPs may depend on nanoparticle concentration, exposure duration, plant species, and experimental conditions. Therefore, longer exposure periods and concentrations above 160 mg/L may help determine whether the observed tendency develops into a clearer growth-inhibitory or phytotoxic response. The corresponding numerical data are provided in Supplementary Table S2.

3.8.2. Chlorophyll, Carotenoid, and Anthocyanin Contents

The measured chlorophyll, total carotenoid, and anthocyanin contents of *Phaseolus vulgaris* leaves exhibited a non-linear pattern across the tested η-type alumina NP concentrations. The highest chlorophyll a, chlorophyll b, total chlorophyll, anthocyanin, and total carotenoid contents were recorded at 40 mg/L, reaching 0.090, 0.139, and 0.229 mg g^{-1} Fresh weight, 0.536 µmol g^{-1} FW, and 0.299 mg g^{-1} FW, respectively. In contrast, the corresponding values at 160 mg/L decreased to 0.014, 0.015, and 0.029 mg g^{-1} FW, 0.061 µmol g^{-1} FW, and 0.056 mg g^{-1} FW, respectively, representing the lowest levels observed among the treatments. At 80 mg/L, pigment contents generally remained close to the untreated control or exceeded the control for some parameters, whereas the 10 and 20 mg/L treatments generally showed lower values. The normalized data are shown in Figure 9, where the pigment parameters followed a non-linear trend with a modest increase from 10 to 20 mg/L and a maximum at 40 mg/L. At 80 mg/L, the responses generally approached or remained slightly above the control level, whereas all pigment parameters markedly declined at 160 mg/L. As all seedlings were grown in the dark and were exposed to laboratory light only briefly during harvesting, these results reflect the relative effects of the NP concentrations on pigment accumulation in etiolated seedlings rather than differences in photosynthetic performance.

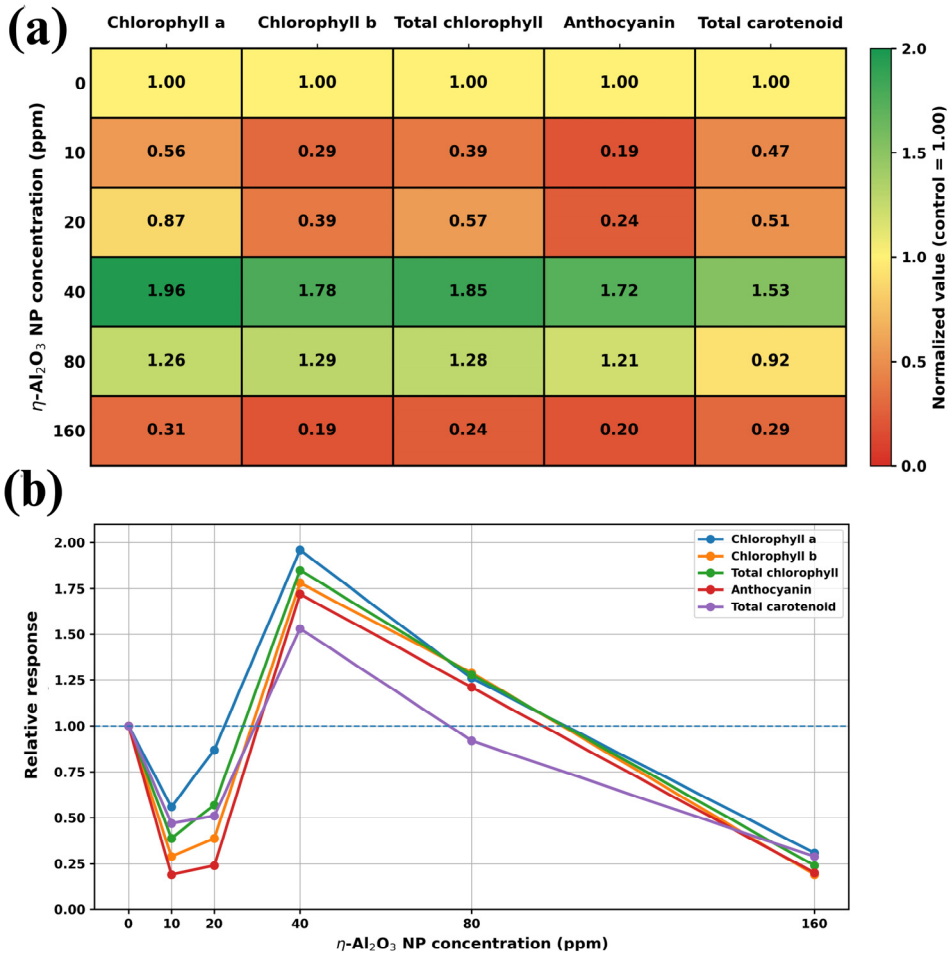

Figure 9. (**a**) Heatmap of pigments, (**b**) line graph of pigments. Values were obtained from a single pooled extract per treatment.

In previous studies conducted with Al_2O_3 NPs, it has been reported that low and medium doses can enhance growth and certain physiological parameters, whereas at high doses, this effect diminishes and turns into toxicity [56]. However, the response

observed in the present study should be distinguished from canonical hormesis, which is typically characterized by low-dose stimulation followed by high-dose inhibition. Here, the measured pigment contents were lower at 10–20 mg/L, higher at 40 mg/L, and lower again at higher concentrations, exhibiting a descriptive multiphasic, non-monotonic pattern rather than a confirmed hormetic response. As the pigment contents were determined from pooled samples, this pattern is presented descriptively, and further studies with replicated measurements are needed to confirm it. In addition, Sedefoglu et al. [37] demonstrated that plant responses to nanoparticle exposure may vary not only with nanoparticle concentration but also with the applied suspension volume, indicating that the effective nanoparticle load is an important determinant of the physiological response.

Similar non-linear changes in plant responses have been reported for other nanoparticles and were related to nanoparticle size and the degree of aggregation [57]. In addition, previous studies have shown that high Al_2O_3 NP exposure can increase ROS production, lipid peroxidation and antioxidant enzyme activities in plants, together with decreases in chlorophyll, carotenoid and anthocyanin contents [58,59]; however, further studies are needed to determine whether such mechanisms are involved in the pigment changes observed in the present study.

Recent studies illustrate how dye-removal performance depends on nanomaterial composition and treatment conditions. A TiO_2–SiO_2–Fe_2O_3 heterojunction system has been examined for sunlight-driven Rhodamine B degradation and catalyst reusability [48]. The evolution of H_2 bubbles during photocatalytic H_2 generation on Ni_2P/CdS nanorods has also been studied, with diffusion, surface renewal and surface chemical reaction reported to govern the growth of long strip bubbles [60]; however, this gas-evolution system is mechanistically distinct from the present dye-decolorization assay. In a different treatment approach, ZrO_2/Pisum sativum nanocomposites have been assessed for Eriochrome Black T adsorption using kinetic modeling and toxicity tests [61]. Because the materials, target compounds, and treatment mechanisms differ, the reported removal efficiencies and kinetic models cannot be directly compared with those of the present UV-irradiated Basic Fuchsin system.

Green-synthesized ZnO/Fe_2O_3 nanocomposites have also been evaluated for photocatalytic and antibacterial activity, with antibacterial responses depending on irradiation conditions [62]. Such findings provide comparative context for the importance of material-specific and assay-specific conditions, without establishing antibacterial activity for the alumina nanoparticles investigated here.

The toxicological evaluation of plant-mediated materials should distinguish the properties of the source plant from those of the final calcined material.

4. Conclusions

In this study, cubic defect-spinel transition alumina nanoparticles, tentatively consistent with η-Al_2O_3, were obtained using a plant extract-mediated synthesis route and evaluated for their structural, optical, photocatalytic, antibacterial, and plant-response properties. XRD indicated a nanostructured cubic defect-spinel transition alumina tentatively consistent with η-Al_2O_3, with an apparent Scherrer crystallite size of 7.31 nm, while SEM showed ~29 nm surface particles assembled into micrometre-scale agglomerates. An exploratory direct-Tauc construction gave an intercept of 5.77 eV, but relative-reflectance normalization and the short-wavelength fitting interval prevent its identification as a validated fundamental band gap. UV irradiation in the presence of the nanoparticles produced 62.18% BF decolorization after 180 min, whereas the parallel dark test showed no measurable net decolorization. Because a UV-only control was not performed, the direct-photolysis and nanoparticle-assisted contributions remain unresolved. The initial 0–60 min interval was approximately

consistent with an apparent pseudo-first-order relation ($k_app = 3.61 \times 10^{-3}$ min^{-1}), while the full profile was nonlinear. Decolorization declined from approximately 62% to 19% over five cycles; catalyst loss and intrinsic deactivation were not separated. The nanoparticles showed no marked antibacterial activity against the tested strains at 12.5–50 mg/mL, which may be partly related to their agglomeration.

In etiolated *Phaseolus vulgaris* seedlings, pigment contents showed a non-monotonic trend, with lower values at 10–20 mg/L, the highest values at 40 mg/L and the lowest values at 160 mg/L, whereas growth and biomass parameters showed no consistent dose-dependent trend. Overall, the plant extract-mediated transition alumina showed UV-induced dye decolorization with limited retention of performance on reuse and descriptive non-monotonic variation in plant pigment contents, rather than marked antibacterial activity under the tested conditions. By combining the synthesis of cubic defect-spinel transition alumina using *Laurus nobilis* pruning waste with photocatalytic, antibacterial and plant-response assessments, this study provides an integrated evaluation of the material obtained by this pruning-waste-mediated route, and the low-dose pigment trend observed here offers a basis for future replicated studies on the agricultural use of alumina nanoparticles. Further limitations of the present work are the tentative phase assignment in the absence of phase-sensitive techniques such as SAED or ^{27}Al MAS NMR, the use of relative rather than absolute diffuse reflectance, the absence of a dark pre-equilibration step before irradiation, and the lack of a catalyst-free UV-only control. These limitations prevent phase-specific mechanistic conclusions and separation of the nanoparticle contribution to decolorization. Future studies should include thermal analysis of the phase evolution of the precursor, specific surface area measurements, post-cycle structural characterization of the catalyst, an assessment of the energy demand of calcination, and longer plant exposure periods with systematic low-dose screening.

Supplementary Materials: The following supporting information can be downloaded at: https://www.mdpi.com/article/10.3390/nano16231513/s1, Table S1: antibacterial; Table S2: nanofertilizer.

Author Contributions: Conceptualization, T.D.; methodology, T.D. and K.V.; software, T.D.; validation, T.D.; formal analysis, T.D. and K.V.; investigation, T.D.; resources, T.D.; data curation, T.D. and K.V.; writing—original draft preparation, T.D. and K.V.; writing—review and editing, T.D.; visualization, T.D. and K.V.; supervision, T.D.; project administration, T.D.; funding acquisition, T.D. All authors have read and agreed to the published version of the manuscript.

Funding: This research was funded by the Scientific Research Projects Unit of Çukurova University, grant number FBA 2026-18699.

Data Availability Statement: The original contributions presented in this study are included in the article and Supplementary Material. Further inquiries can be directed to the corresponding author.

Acknowledgments: This interdisciplinary study was designed within the scope of strengthening university–university collaboration.

Conflicts of Interest: The authors declare no conflicts of interest.

References

1. Lellis, B.; Fávaro-Polonio, C.Z.; Pamphile, J.A.; Polonio, J.C. Effects of textile dyes on health and the environment and bioremediation potential of living organisms. *Biotechnol. Res. Innov.* **2019**, *3*, 275–290. [CrossRef]
2. United Nations General Assembly. *Transforming Our World: The 2030 Agenda for Sustainable Development*; Resolution A/RES/70/1; United Nations: New York, NY, USA, 2015. Available online: https://sdgs.un.org/2030agenda (accessed on 31 October 2026).
3. Langsdorf, A.; Volkmar, M.; Holtmann, D.; Ulber, R. Material utilization of green waste: A review on potential valorization methods. *Bioresour. Bioprocess.* **2021**, *8*, 19. [CrossRef] [PubMed]
4. Jwad, K.H.; Saleh, T.H.; Abd-Alhamza, B. Preparation of aluminum oxide nanoparticles by laser ablation and a study of their applications as antibacterial and wounds healing agent. *Nano Biomed. Eng.* **2019**, *11*, 313–319. [CrossRef]

5. Santo, D.; Rodarte, M.; Andreto, C.; Cavaleiro, D.; Carvalho, I.; Balestra, R.; Carvalho, S. Multifunctional alumina scaffolds with enhanced bioactivity and antimicrobial properties for bone tissue engineering. *Ceram. Int.* **2025**, *51*, 6155–6165. [CrossRef]
6. Laskar, I.; Saha, R. Synthesis of aluminum oxide nanoparticles using seeds of Carica papaya and evaluation of it for antimicrobial, antioxidant, and photocatalysis activity. *J. Anal. Sci. Technol.* **2024**, *15*, 52. [CrossRef]
7. Tran, G.T.; Nguyen, N.T.H.; Nguyen, N.T.T.; Nguyen, T.T.T.; Nguyen, D.T.C.; Tran, T.V. Plant extract-mediated synthesis of aluminum oxide nanoparticles for water treatment and biomedical applications: A review. *Environ. Chem. Lett.* **2023**, *21*, 2417–2439. [CrossRef]
8. Wefers, K.; Misra, C. *Oxides and Hydroxides of Aluminum*; Alcoa Technical Paper No. 19, Revised; Alcoa Research Laboratories: Pittsburgh, PA, USA, 1987.
9. Pecharromán, C.; González-Carreño, T.; Iglesias, J.E. The infrared dielectric properties of η-Al_2O_3. *J. Mater. Res.* **1996**, *11*, 127–133. [CrossRef]
10. Pandey, R.; Vishwakarma, V. Green synthesis of metal-based nanoparticles using *Aloe vera* (L.) Burm.f: A review. *Discov. Chem.* **2026**, *3*, 122. [CrossRef]
11. Anuar, M.S.K.; Che Abdullah, C.A.; Nazarudin, M.F.; Ishaq, S.I.; Azmai, M.N.A.; Salleh, A.; Md Yasin, I.S.; Yusof, M.T. *Talaromyces purpureogenus*-mediated mycosynthesis of aluminium oxide nanoparticles and characterization of the physicochemical properties at different calcination temperatures. *Fungal Biol.* **2025**, *129*, 101570. [CrossRef] [PubMed]
12. Ikhioya, I.L.; Nkele, A.C. Green synthesis and characterization of aluminum oxide nanoparticle using neem leaf extract (Azadirachta Indica). *Hybrid Adv.* **2024**, *5*, 100141. [CrossRef]
13. Mahdi, W.K.; Flayyih, A.O.; Musa, F.H. Green Synthesis, Characterization, and Applications of Aluminum Oxide Nanoparticles Using Aqueous Extract of Clove. *J. Kim. Val.* **2024**, *10*, 277–289. [CrossRef]
14. Koopi, H.; Buazar, F. A novel one-pot biosynthesis of pure alpha aluminum oxide nanoparticles using the macroalgae *Sargassum ilicifolium*: A green marine approach. *Ceram. Int.* **2018**, *44*, 8940–8945. [CrossRef]
15. Saleh, A.K.; Shaban, A.S.; Diab, M.A.; Debarnot, D.; Elzaref, A.S. Green synthesis and characterization of aluminum oxide nanoparticles using Phoenix dactylifera seed extract along with antimicrobial activity, phytotoxicity, and cytological effects on *Vicia faba* seeds. *Biomass Convers. Biorefin.* **2024**, *14*, 31859–31875. [CrossRef]
16. Dhawale, V.P.; Late, D.J.; Kulkarni, S.D. Synthesis, characterization of α-Al_2O_3 nanoparticles and its application in decolorization of methyl orange azo dye in the presence of UV light. *J. Nanosci. Technol.* **2019**, *5*, 580–583. [CrossRef]
17. Atrak, K.; Ramazani, A.; Taghavi Fardood, S. Green synthesis of amorphous and gamma aluminum oxide nanoparticles by tragacanth gel and comparison of their photocatalytic activity for the degradation of organic dyes. *J. Mater. Sci. Mater. Electron.* **2018**, *29*, 8347–8353. [CrossRef]
18. Nogueira, F.G.E.; Asencios, Y.J.O.; Rodella, C.B.; Porto, A.L.M.; Assaf, E.M. Alternative route for the synthesis of high surface-area η-Al_2O_3/Nb_2O_5 catalyst from aluminum waste. *Mater. Chem. Phys.* **2016**, *184*, 23–30. [CrossRef]
19. Gholizadeh, Z.; Aliannezhadi, M.; Ghominejad, M.; Shariatmadar Tehrani, F. Novel boehmite and η-alumina nanostructures synthesized using a green ultrasonic-assisted hydrothermal method by clove extract for water treatment. *J. Water Process Eng.* **2024**, *65*, 105786. [CrossRef]
20. Busca, G. The surface of transitional aluminas: A critical review. *Catal. Today* **2014**, *226*, 2–13. [CrossRef]
21. Sadak, M.S. Impact of silver nanoparticles on plant growth, some biochemical aspects, and yield of fenugreek plant (*Trigonella foenum-graecum*). *Bull. Natl. Res. Cent.* **2019**, *43*, 38. [CrossRef]
22. van Dijk, M.; Morley, T.; Rau, M.L.; Saghai, Y. A meta-analysis of projected global food demand and population at risk of hunger for the period 2010–2050. *Nat. Food* **2021**, *2*, 494–501. [CrossRef] [PubMed]
23. Javed, M.; Iqbal, S.; Qamar, M.A.; Shariq, M.; Ahmed, I.A.; BaQais, A.; Alzahrani, H.; Ali, S.K.; Masmali, N.A.; Althagafi, T.M.; et al. Fabrication of Effective Co-SnO_2/SGCN Photocatalysts for the Removal of Organic Pollutants and Pathogen Inactivation. *Crystals* **2023**, *13*, 163. [CrossRef]
24. Prashanth, P.A.; Raveendra, R.S.; Hari Krishna, R.; Ananda, S.; Bhagya, N.P.; Nagabhushana, B.M.; Lingaraju, K.; Raja Naika, H. Synthesis, characterizations, antibacterial and photoluminescence studies of solution combustion-derived α-Al_2O_3 nanoparticles. *J. Asian Ceram. Soc.* **2015**, *3*, 345–351. [CrossRef]
25. Dassanayake, T.M.; Dassanayake, A.C.; Abeydeera, N.; Pant, B.D.; Jaroniec, M.; Kim, M.H.; Huang, S.D. An aluminum lining to the dark cloud of silver resistance: Harnessing the power of potent antimicrobial activity of γ-alumina nanoparticles. *Biomater. Sci.* **2021**, *9*, 7996–8006. [CrossRef] [PubMed]
26. Davis, P.H. (Ed.) *Flora of Turkey and the East Aegean Islands*; Edinburgh University Press: Edinburgh, UK, 1982; Volume 7.
27. Mukunthan, K.S.; Balaji, S. Cashew apple juice (*Anacardium occidentale* L.) speeds up the synthesis of silver nanoparticles. *Int. J. Green Nanotechnol. Biomed.* **2012**, *4*, 71–79. [CrossRef]
28. Sharma, D.; Kanchi, S.; Bisetty, K. Biogenic synthesis of nanoparticles: A review. *Arab. J. Chem.* **2019**, *12*, 3576–3600. [CrossRef]
29. Pacewska, B.; Keshr, M. Thermal transformations of aluminium nitrate hydrate. *Thermochim. Acta* **2002**, *385*, 73–80. [CrossRef]

30. Singh, K.R.B.; Singh, P.; Singh, J.; Pandey, S.S. Nanobioengineered Al_2O_3 core–shell nanoparticle preparation using Bauhinia Variegate plant extract for efficient photocatalysis and electrochemical sensing. *ACS Appl. Bio Mater.* **2024**, *7*, 7646–7658. [CrossRef] [PubMed]
31. Castro, M.; Tous, L.; Herrera, A.; Martinez-Bernett, D.; Saba, M. Effect of aluminum salt precursor on the crystalline structure of alumina nanoparticles (Al_2O_3) synthesized by green chemistry using *Cymbopogon citratus* extract. *Processes* **2025**, *13*, 3876. [CrossRef]
32. Ahmad, A.; Javed, M.S.; Khan, M.; Ahmad, I.; Almarhoon, Z.M.; Sheikh, M.; Afzal, A.M.; Nazir, A.; Park, S.J.; Choi, D. Green fabrication of γ-Al_2O_3 bionanomaterials using *Coriandrum sativum* plant extract and its photocatalytic and antibacterial activity. *Nanotechnol. Rev.* **2026**, *15*, 20250187. [CrossRef]
33. Mekasuwandumrong, O.; Pavarajarn, V.; Inoue, M.; Praserthdam, P. Preparation and phase transformation behavior of χ-alumina via solvothermal synthesis. *Mater. Chem. Phys.* **2006**, *100*, 445–450. [CrossRef]
34. Louaer, S.; Wang, Y.; Guo, L. Fast synthesis and size control of gibbsite nanoplatelets, their pseudomorphic dehydroxylation, and efficient dye adsorption. *ACS Appl. Mater. Interfaces* **2013**, *5*, 9648–9655. [CrossRef] [PubMed]
35. Dogan, T. Assessment of the wastewater treatment performance of neodymium-doped Al_2O_3 nanoparticles under UV irradiation. *Appl. Sci.* **2026**, *16*, 3773. [CrossRef]
36. Ari, S.; Das, S. A comprehensive investigation from sprouts to microgreens and mature plants of *Amaranthus viridis* L. as a prospective natural inhibitor of xanthine oxidase enzyme. *Discov. Food* **2025**, *5*, 135. [CrossRef]
37. Sedefoglu, N.; Zalaoglu, Y.; Bozok, F. Green synthesized ZnO nanoparticles using *Ganoderma lucidum*: Characterization and in vitro nanofertilizer effects. *J. Alloys Compd.* **2022**, *918*, 165695. [CrossRef]
38. Sun, R.; Shen, S.; Zhang, D.; Ren, Y.; Fan, J. Hydrofining of coal tar light oil to produce high octane gasoline blending components over γ-Al_2O_3- and η-Al_2O_3-supported catalysts. *Energy Fuels* **2015**, *29*, 7005–7013. [CrossRef]
39. Tilley, D.B.; Eggleton, R.A. The natural occurrence of eta-alumina (η-Al_2O_3) in bauxite. *Clays Clay Miner.* **1996**, *44*, 658–664. [CrossRef]
40. Stumpf, H.C.; Russell, A.S.; Newsome, J.W.; Tucker, C.M. Thermal transformations of aluminas and alumina hydrates—Reaction with 44% technical acid. *Ind. Eng. Chem.* **1950**, *42*, 1398–1403. [CrossRef]
41. Zhou, R.S.; Snyder, R.L. Structures and transformation mechanisms of the η, γ and θ transition aluminas. *Acta Crystallogr. Sect. B* **1991**, *47*, 617–630. [CrossRef]
42. Rashid, S.N.; Bdewi, S.F.; Alshammary, E.T.; Hammad, R.T. Characterization of alumina nanoparticles prepared via green synthesis method. *J. Univ. Anbar Pure Sci.* **2023**, *17*, 184–189. [CrossRef]
43. Abbas, L.K.; Jubier, N.J.; Al-Ogaili, H.A.A.T. Al_2O_3 Nanoparticles Synthesized Using Plant Extracts: Characterization and Application to Glucose Sensing. *Dig. J. Nanomater. Biostruct.* **2026**, *21*, 55196. [CrossRef]
44. Farajimotlagh, M.; Poursalehi, R.; Aliofkhazraei, M. Synthesis mechanisms, optical and structural properties of η-Al_2O_3 based nanoparticles prepared by DC arc discharge in environmentally friendly liquids. *Ceram. Int.* **2017**, *43*, 7717–7723. [CrossRef]
45. Kubelka, P.; Munk, F. Ein Beitrag zur Optik der Farbanstriche. *Z. Tech. Phys.* **1931**, *12*, 593–601.
46. Tauc, J.; Grigorovici, R.; Vancu, A. Optical properties and electronic structure of amorphous germanium. *Phys. Status Solidi B* **1966**, *15*, 627–637. [CrossRef]
47. Rajendran, S.; Palani, G.; Shanmugam, V.; Trilaksanna, H.; Kannan, K.; Nykiel, M.; Korniejenko, K.; Marimuthu, U. A review of synthesis and applications of Al_2O_3 for organic dye degradation/adsorption. *Molecules* **2023**, *28*, 7922. [CrossRef] [PubMed]
48. Tebbi, S.O.; Amrane, A.; Boudraa, R.; Bollinger, J.-C.; Salvestrini, S.; Kanjal, M.I.; Tiri, A.; Belkhiri, L.; Alharthi, M.N.; Mouni, L. Green Synthesis of Sustainable and Cost-Effective TiO_2-SiO_2-Fe_2O_3 Heterojunction Nanocomposites for Rhodamine B Dye Degradation Under Sunlight. *Water* **2025**, *17*, 168. [CrossRef]
49. Sadiq, I.M.; Chowdhury, B.; Chandrasekaran, N.; Mukherjee, A. Antimicrobial sensitivity of *Escherichia coli* to alumina nanoparticles. *Nanomedicine* **2009**, *5*, 282–286. [CrossRef] [PubMed]
50. Sikora, P.; Augustyniak, A.; Cendrowski, K.; Nawrotek, P.; Mijowska, E. Antimicrobial activity of Al_2O_3, CuO, Fe_3O_4, and ZnO nanoparticles in scope of their further application in cement-based building materials. *Nanomaterials* **2018**, *8*, 212. [CrossRef] [PubMed]
51. Hassan Basri, H.; Talib, R.A.; Sukor, R.; Othman, S.H.; Ariffin, H. Effect of synthesis temperature on the size of ZnO nanoparticles derived from pineapple peel extract and antibacterial activity of ZnO–starch nanocomposite films. *Nanomaterials* **2020**, *10*, 1061. [CrossRef] [PubMed]
52. Rokbani, H.; Daigle, F.; Ajji, A. Combined effect of ultrasound stimulations and autoclaving on the enhancement of antibacterial activity of ZnO and SiO_2/ZnO nanoparticles. *Nanomaterials* **2018**, *8*, 129. [CrossRef] [PubMed]
53. Simonin, M.; Richaume, A. Impact of engineered nanoparticles on the activity, abundance, and diversity of soil microbial communities: A review. *Environ. Sci. Pollut. Res.* **2015**, *22*, 13710–13723. [CrossRef] [PubMed]

54. de Almeida, G.H.G.; Siqueira-Soares, R.d.C.; Mota, T.R.; de Oliveira, D.M.; Abrahão, J.; de Paiva Foletto-Felipe, M.; dos Santos, W.D.; Ferrarese-Filho, O.; Marchiosi, R. Aluminum oxide nanoparticles affect the cell wall structure and lignin composition slightly altering the soybean growth. *Plant Physiol. Biochem.* **2021**, *159*, 335–346. [CrossRef] [PubMed]
55. Chahardoli, A.; Karimi, N.; Chaichi, M. The bilateral effects of Al_2O_3NPs on *Dracocephalum kotschyi* Boiss: Insights from physiological responses, antioxidant defense efficacy, and phytochemical yield. *BMC Plant Biol.* **2026**, *26*, 1128. [CrossRef] [PubMed]
56. Amist, N.; Singh, N.B.; Yadav, K.; Singh, S.C.; Pandey, J.K. Comparative studies of Al^{3+} ions and Al_2O_3 nanoparticles on growth and metabolism of cabbage seedlings. *J. Biotechnol.* **2017**, *254*, 1–8. [CrossRef] [PubMed]
57. Konate, A.; Wang, Y.; He, X.; Adeel, M.; Zhang, P.; Ma, Y.; Ding, Y.; Zhang, J.; Yang, J.; Kizito, S.; et al. Comparative effects of nano and bulk-Fe_3O_4 on the growth of cucumber (*Cucumis sativus*). *Ecotoxicol. Environ. Saf.* **2018**, *165*, 547–554. [CrossRef] [PubMed]
58. Yanık, F.; Vardar, F. Oxidative stress response to aluminum oxide (Al_2O_3) nanoparticles in *Triticum aestivum*. *Biologia* **2018**, *73*, 129–135. [CrossRef]
59. Owji, H.; Hemmati, S.; Heidari, R.; Hakimzadeh, M. Effect of alumina (Al_2O_3) nanoparticles and macroparticles on *Trigonella foenum-graceum* L. in vitro cultures: Assessment of growth parameters and oxidative stress-related responses. *3 Biotech* **2019**, *9*, 419. [CrossRef] [PubMed]
60. Lu, X.; Wang, X.; Fu, X.; Yang, K.; Zheng, X.; Lin, W.; Wang, W.; Wang, S. Kinetics study of H_2 bubble evolution in photocatalytic H_2 generation on Ni_2P/CdS nanorods. *Int. J. Hydrogen Energy* **2025**, *193*, 152462. [CrossRef]
61. Kanjal, M.I.; Muneer, M.; Ullah, S.; Fayyaz, M.; Nadeem, R.; Ahamad, M.I.; Zulqarnain, R.M.; Habib, M.A.; Ibrahim, A.B.M. Kinetic modeling and toxicological assessment of Eriochrome Black T dye: Enhanced adsorptive approach using novel ZrO_2/Pisum sativum nanocomposites. *J. Iran. Chem. Soc.* **2025**, *22*, 1991–2004. [CrossRef]
62. Mouni, L.; Rai, A.; Tabchouche, N.; Silem, A.; Guellati, I.; Mousli, G.; Kanjal, M.I.; Assadi, A.A.; Fadhillah, F.; Ali, F.A.A.; et al. Green synthesis of ZnO/Fe_2O_3 nanocomposites using *Urtica dioica* extract: Evaluation of photocatalytic, antioxidant, and antibacterial activities. *Catalysts* **2026**, *16*, 276. [CrossRef]

Disclaimer/Publisher's Note: The statements, opinions and data contained in all publications are solely those of the individual author(s) and contributor(s) and not of MDPI and/or the editor(s). MDPI and/or the editor(s) disclaim responsibility for any injury to people or property resulting from any ideas, methods, instructions or products referred to in the content.